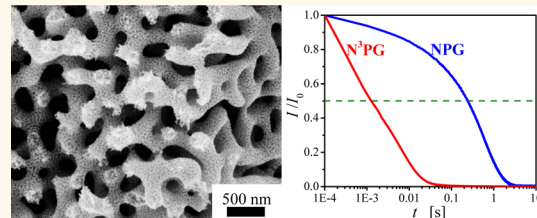


Hierarchical Nested-Network Nanostructure by Dealloying

Zhen Qi[†] and Jörg Weissmüller^{†,‡,*}

[†]Institute of Materials Physics, Hamburg University of Technology, Hamburg, Germany, and [‡]Institute of Materials Research, Materials Mechanics, Helmholtz-Zentrum Geesthacht, Geesthacht, Germany

ABSTRACT Applications of porous microstructures in functional materials often impose conflicting requirements on the pore size, which may be met by hierarchical structures that combine porosity on distinctly different length scales. Here we report an electrochemical dealloying strategy that yields bulk samples of porous gold with a hierarchical microstructure. A nanoscale network of solid ligaments forms the lower hierarchy level, which is nested within the geometrically similar, but much larger, network of the upper hierarchy level. Starting from a dilute solid solution of Au in Ag, controlled electrochemical corrosion yields nanoporous Ag–Au alloy as an intermediate product. Coarsening of the porous alloy creates the large ligaments of the upper hierarchy level. Those are then again dealloyed, which creates the fine ligaments of the lower hierarchy level. We show that the material exhibits enhanced charge transport kinetics while maintaining a large specific surface area.



KEYWORDS: dealloying · nanoporous metals · hierarchical structure · charge transport

Nanoporous metals made by dealloying, in other words by the removal of the less noble component from a solid solution *via* controlled corrosion, take the form of bulk samples with a network structure of nanoscale “ligaments” of uniform size that can be tuned between a few nanometers and several micrometers.^{1–3} The solid network is interpenetrated by a complementary and geometrically similar open pore network. The prospect of using these structures in novel functional materials rests on their large specific surface area, which is accessible to electric or chemical signals. For instance, filling the pore space with electrolyte and biasing it against a counter electrode leads to ionic transport and the polarization of the electrochemical double-layer along the entire pore surface. This allows the material to respond to external stimuli, which tune the local surface state and, thereby, the entire materials behavior. The network structure that is created by dealloying is attractive for materials design since the solid skeleton carries load³ and since the low tortuosity of the pore space favors efficient transport. On the way to novel functional materials, applications as electrochemically or chemically driven actuators,^{4–6} materials with switchable strength and ductility,⁷ varistors,⁸ and catalysts^{9–12}

are under investigation. The two key aspects of the materials design strategy, namely, (i) large specific surface area for functionalization and (ii) rapid transport pathways for fast switching, are inherently competing since large area requires small pore size, impeding fast transport of ions. The obvious solution to this dilemma is structural hierarchy. An optimal porous functional material would benefit from at least two levels of pore size, extremely small pores for function and a network of larger pores for transport. In fact, hierarchy is ubiquitous in nature and society wherever functional centers are distributed and need to be interlinked by efficient transport pathways. Here, we report a strategy which generates porous gold samples with a two-level, hierarchical microstructure that consists of self-similar, nested-networks on two distinct, but well-defined, length scales. We show that the material combines high surface area with rapid transport.

Bimodal nanoporous structures can be created by dealloying multiphase master alloys.^{13,14} In such materials, the geometry of the smaller pores is characteristic of the low tortuosity, interlinked network structure of dealloying, whereas the larger pores replicate the microstructure of the master alloy, with a less ordered architecture. The need for rapid solidification of the master

* Address correspondence to weissmueller@tuhh.de.

Received for review April 2, 2013
and accepted June 21, 2013.

Published online June 21, 2013
10.1021/nn4021345

© 2013 American Chemical Society

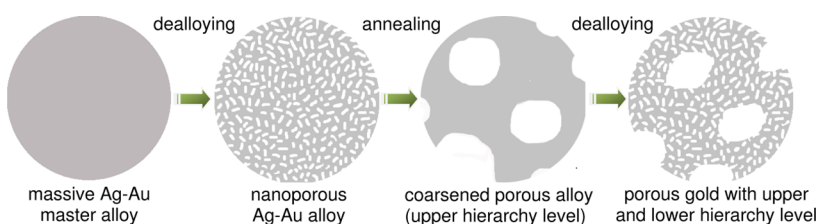


Figure 1. Schematic diagram illustrating the strategy toward hierarchical nanoporous gold.

alloy restricts the approach to thin foils. Nanoporous gold (NPG) with a bimodal pore size distribution that exhibits the network structure on both scales has been prepared using a sequence of corrosion—coarsening—Ag plating—realloying—corrosion.¹⁵ Because that method relies on a diffusion process during plating, it was applied to 100 nm thin porous membranes rather than bulk samples. Recently, a somewhat similar approach was applied to thin wires of Cu—Au.¹⁶ Again, the limited diffusion range prevents the application to samples with macroscopic dimension. It has been suggested to prepare macroscopic samples of hierarchical nanoporous gold by two-step dealloying, starting from a homogeneous ternary precursor alloy and removing first the least noble component and only later the intermediate one.¹⁷ Yet, as miscibility gaps tend to prevent homogenization, suitable ternary alloy systems that can be formed as uniform bulk solid solutions have yet to be identified.

The present strategy, as illustrated in Figure 1, generates bulk samples of hierarchical porous metal by starting from a Ag—Au solid solution. Whereas the standard approach to NPG is to corrode an alloy with a Au molar fraction, x_{Au} , below but near the parting limit of $x_{\text{Au}} \sim 0.45$, we start out from a considerably more dilute solution of Au in the less noble element (LNE), Ag. Previous work¹⁸ has shown that a considerable amount of LNE (in this instance, Cu) is retained when electrochemically dealloying dilute Cu—Au near the critical dealloying potential. The starting hypothesis and distinguishing aspect of our approach is that careful control of the dealloying potential allows one to increase the amount of residual Ag in the porous material to such an extent that a later, second corrosion step at higher potential becomes possible. The initial corrosion thus creates a nanoporous Ag—Au alloy rather than NPG. The material in this intermediate state is thermally coarsened to form a porous alloy with ~ 200 nm pore size, the upper hierarchy level. The second dealloying step then removes the Ag completely, establishing the lower hierarchy level in the form of nanoporosity within each larger ligament. The sequence of corrosion—coarsening—corrosion for creating a hierarchical pore structure is the distinctive feature of our synthesis. While standard dealloying protocols create almost pure NPG, we deliberately control the initial corrosion process so as to retain a large Ag fraction throughout the nanoporous alloy.

Contrary to the redeposition of Ag that has been used before for creating small volumes of nanoporous Ag—Au, our strategy is applicable to macroscopic samples.

RESULTS

We start out by inspecting the corrosion behavior of master alloys $\text{Ag}_{1-x}\text{Au}_x$ with the Au fraction extending from a more concentrated alloy with $x_{\text{Au}} = 0.25$ down to the dilute $x_{\text{Au}} = 0.05$, focusing first on the critical dealloying potential, E_C . Two approaches toward E_C have been discussed in the literature.^{19–22} One approach rests on anodic polarization curves, identifying E_C with the potential at current density $j = 1 \text{ mA/cm}^2$. The second approach uses chronoamperometry to identify the lowest potential that gives a steady corrosion current over extended periods of time. That potential marks the transition from passivation to formation of a bicontinuous porous structure. For ease of distinction, we designate the first measure for E_C the “massive dealloying potential” (MDP) and the second as “loss of passivation potential” (LPP). Figure 2a,b shows the two measures of E_C for master alloys with Au molar fractions of 5, 10, and 15%. It is apparent that the two definitions yield considerably different values of E_C . This applies especially to the alloys with more Au, where the difference exceeds 100 mV.

Samples were dealloyed at various potentials, E_D , above their LPP, and Figure 2c shows the resulting residual Ag content, $x_{\text{Ag},\text{res}}$ plotted versus E_D . The master alloys with 10 and 15 atom % Au yield $x_{\text{Ag},\text{res}} \approx 10$ atom %, similar to previous reports for Cu—Au¹⁸ and too small for our intended two-step dealloying strategy. By contrast, $x_{\text{Ag},\text{res}}$ in the $\text{Ag}_{95}\text{Au}_5$ increases from 11 to 48 atom % when E_D is decreased from 600 to 300 mV. This brings the composition of the nanoporous Au—Ag alloy close to the parting limit.

We now focus on those latter samples, that is, on the high Ag content nanoporous Au—Ag samples prepared by dealloying $\text{Ag}_{95}\text{Au}_5$ at 300 mV. The high Ag content suggests the possibility of a second dealloying step, as envisaged in the strategy of Figure 1. Figure 3a–c displays overview SEM images of the microstructure in the corresponding stages of preparation. The as-dealloyed material (Figure 3a) is a nanoporous $\text{Ag}_{48}\text{Au}_{52}$ alloy with a ligament size of ~ 16 nm. Upon annealing at 300°C for 3 h, this microstructure coarsens to reach a ligament size of ~ 200 nm. Figure 3b

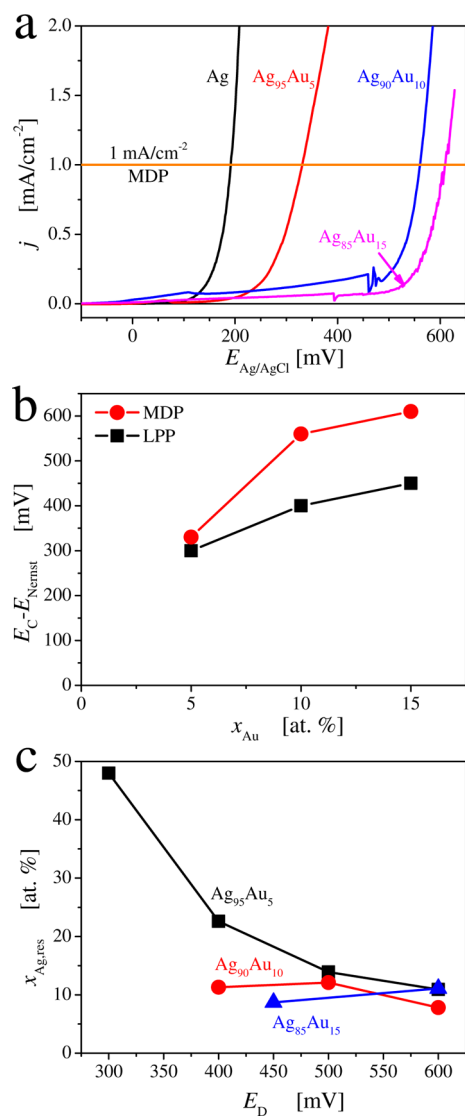


Figure 2. Signatures of the corrosion behavior of pure Ag and of the master alloys $\text{Ag}_{95}\text{Au}_5$, $\text{Ag}_{90}\text{Au}_{10}$, and $\text{Ag}_{85}\text{Au}_{15}$ in 1 M HClO_4 . (a) Current/potential graphs at a scan rate 1 mV/s. (b) Overpotential (relative to the Nernst potential, E_{Nernst} of pure Ag) at loss of passivation (LPP) and at massive dealloying (MDP) versus the Au fraction, x_{Au} , in the master alloy. (c) Residual Ag content, $x_{\text{Ag},\text{res}}$, versus dealloying potential, E_D , for dealloyed material made from the master alloys indicated.

displays this state, in which the upper hierarchy level is already expressed. In order to form the lower hierarchy level, the coarsened porous Ag–Au alloy is subjected to the second dealloying step. We here use $E_D = 750$ mV, similar to what is typically used for dealloying massive Ag–Au. Figure 3c shows the resulting, final microstructure. As can be seen in Figure 3c, the microstructure after the second corrosion step consists of a fine network of nanoscale ligaments nested within each ligament of the coarser network structure. Figure 4a shows details of the final microstructure. The two hierarchy levels of the nested-network structure of the solid are reflected in a complementary and geometrically similar pore channel structure, with ~ 200 nm size upper hierarchy channels and ~ 15 nm size lower hierarchy channels.

Our reference to the nested-network structure as “hierarchical” is suggested by the presence of the two well-defined length scales. As is visible in Figure 4, the sizes of the two levels are not only well separated, but the topology on each of the two levels is geometrically similar to that on the other. A cross-section view of an upper hierarchy level ligament is highlighted in Figure 4b. The micrograph confirms that the entire ligament is porous and composed of lower hierarchy level ligaments. While microstructures with a wide range of sizes or with a bimodal size distribution are indeed widespread in materials science, the hierarchical nested-network structure of the present material follows an unusually stringent design. We also note that the presence of continuous pore channels with low tortuosity on each scale appears particularly suited for efficient transport, a key incentive for our study.

Optical micrographs of the macroscopic sample geometry in different preparation stages are shown in insets of Figure 3a–c. Comparing sample dimensions before and after the corrosion, we find a volume contraction to $\sim 39\%$ of the original size during the first dealloying step. This is larger than what has been reported for the corrosion of $\text{Ag}_{75}\text{Au}_{25}$ in ref 23. Similar to that study, we find the formation of cracks, here at the scale of 20–100 μm . The following preparation steps do

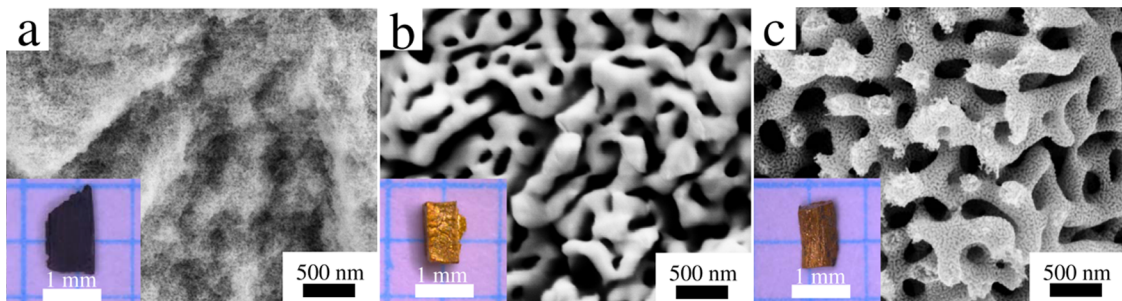


Figure 3. Overview scanning electron micrographs showing microstructure evolution through the consecutive synthesis steps. (a) Fracture surface of as-dealloyed nanoporous $\text{Au}_{52}\text{Ag}_{48}$ sample after first dealloying step. (b) Fracture surface of annealed sample showing coarsened ligaments. (c) Hierarchical structure formed after second dealloying step.

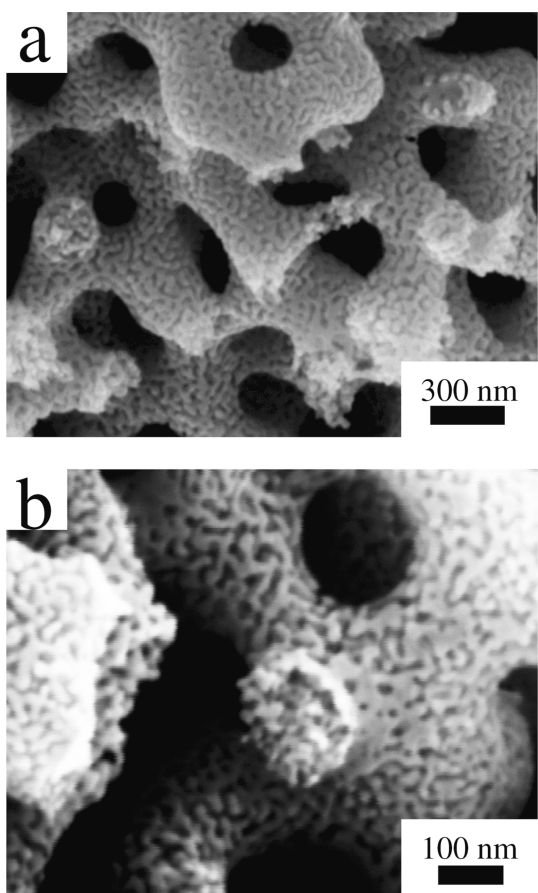


Figure 4. Scanning electron micrographs showing details of nested-network microstructure formed during second dealloying step. (a) Upper and lower hierarchy level networks. (b) Cross section of a fractured upper hierarchy level ligament, illustrating that the lower-level network penetrates the entire upper-level ligament.

not give rise to noticeable extra shrinkage or cracking. As can be seen in Figure 3c, the final nested-network structure takes the form of a monolithic bulk sample.

The net surface area of the nested-network nanoporous gold (N^3PG) samples can be measured by means of the electrochemical capacitance ratio method.²⁴ Figure 5a shows cyclic voltammograms (CVs) in the double-layer region at different scan rates. The corresponding averages of the capacitive currents, I_c , at the center of the CVs are shown in Figure 4b. The current values scale with the potential scan rate, implying that the mass-specific surface area, α_m , may be determined as outlined above. For N^3PG , we find $\alpha_m = 3.0 \pm 0.1 \text{ m}^2/\text{g}$. By means of comparison, we have also investigated a NPG sample made by conventional, one-step dealloying. This sample is nanoporous but lacks the upper hierarchy level. The results in Figure 4 imply $\alpha_m = 4.0 \pm 0.1 \text{ m}^2/\text{g}$.

As a test for the impact of the structural hierarchy on the ion transport kinetics in the pore space, we performed a series of step potential measurements, comparing the kinetics of double-layer charging in N^3PG and in a NPG reference sample. The capacitance ratio

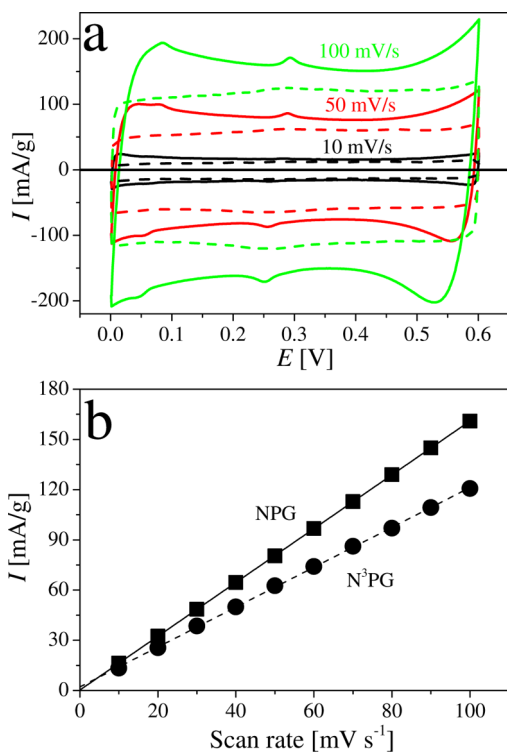


Figure 5. Electrochemical characterization of nanoporous gold (NPG) and nested-network nanoporous gold (N^3PG). (a) Cyclic voltammograms of current I versus electrode potential E in the nominally capacitive regime using different scan rates as labeled in the figures. Solid lines, NPG; dashed lines, N^3PG . (b) Mean current magnitude, I_c , at $E = 0.3 \text{ V}$ versus the scan rate. The data allow estimates of the mass-specific surface area.

data of the previous paragraph show that these samples had comparable specific surface area values and, therefore, comparable ligament size (at the lower hierarchy level in the case of N^3PG). The sample size of N^3PG in this experiment was $0.7 \times 0.7 \times 1.6 \text{ mm}^3$, while that of NPG was $0.9 \times 0.9 \times 1.8 \text{ mm}^3$. Figure 6a,b shows current transients after potential steps. On the log–linear scale of the figures, the graphs of current versus time exhibit points of inflection. Studies of transport kinetics of planar gold electrode surfaces show closely similar behavior (yet with much shorter time constants); the inflection points there separate regimes in which the diffusion of different ions controls the kinetics.²⁵ Irrespective of these details, the data show that under all conditions the current decay in N^3PG is strongly accelerated as compared to that in NPG. For instance, when the potential is stepped within the double-layer region, the current in N^3PG has decayed to half of its initial value in less than 2 ms. By contrast, NPG reaches the same state after about 0.3 s. In the oxygen adsorption region, N^3PG needs $\sim 1 \text{ s}$ for the current to reach its final inflection point, while NPG needs $\sim 100 \text{ s}$. In other words, the charging kinetics in N^3PG is faster, by factors of 150 in the double-layer region and 100 in the oxygen species adsorption region, compared with NPG. As a particularly simple

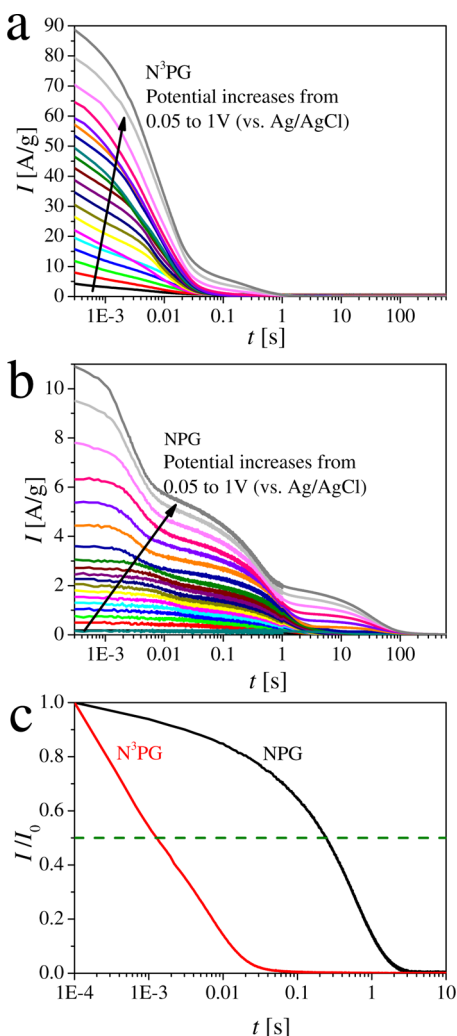


Figure 6. Charging kinetics of the porous materials. Transients of current, I , versus time, t , following potential steps from starting electrode potential $E_0 = 0\text{ V}$ to final potential E_F . Graphs in (a) and (b) show experiments with E_F increasing from 0.05 to 1 V with an increment of 0.05 V . Note the different charging kinetics in capacitive versus oxygen species electrosorption regimes. Graphs in (c) compare current transients after jumping from $E_0 = 0.1\text{ V}$ to $E_F = 0.2\text{ V}$ for the two materials. Charging kinetics may be measured by time, $t_{1/2}$, required for charging current I to decay to 50% of the initial current, I_0 . Dashed line indicates $I/I_0 = 0.5$.

process, Figure 6c inspects a potential jump from 0.1 to 0.2 V within the double-layer region in detail. The graphs represent chronoamperometry results of current versus time for N³PG and NPG. The time, $t_{1/2}$, for I to decay to 50% of its initial value is a measure for the transport kinetics and for the switching rate in applications as an electrochemically functionalized material. We find that $t_{1/2} = 1.3\text{ ms}$ for N³PG, which is nearly 200 times faster than the 250 ms in NPG.

DISCUSSION

Our findings for the less noble element (LNE) retention during dealloying of dilute solid solutions at low overpotential connect to the underlying mechanisms and driving forces of dealloying. As a prerequisite for

enabling the second dealloying step, which is inherent to our strategy, sufficient LNE retention is also the key to our synthesis strategy. This motivates the focus, in our discussion, on LNE retention.

Ateya *et al.* have studied the corrosion of dilute noble metal alloys, focusing on the example of Cu–Au.^{26,27} These authors observed a critical dealloying potential only for $x_{\text{Au}} > 0.1$. Yet, in their study of Ag–Au, Sieradzki *et al.*¹⁹ report critical dealloying potentials for x_{Au} as low as 0.05 , in agreement with the present findings. The results by Ateya *et al.*^{26,27} do agree with our findings inasmuch as the retention of a considerable less noble element fraction is found after dealloying of dilute solutions, including Cu₉₅Au₅. The observations have been discussed in terms of pore walls that are Au-rich rather than pure Au.²⁶ In that respect, it is noteworthy that dilute solutions can be dealloyed at low overpotential. In acidic solution, they are then likely free of oxygen adsorbate layers so that surface diffusion and, hence, coarsening behind the dealloying front are fast. This in turn implies the exposure of LNE atoms from the native alloy in the interior of the original ligaments to further dissolution. The high LNE retention in the experiment is therefore remarkable.

The LNE retention is more readily reconciled with the established observations when one adopts a phenomenological point of view. As the alloy becomes more concentrated in Au, the Nernst potential, E_{Nernst} , of the LNE will increase and the driving force for dissolution decrease. For any given value of E_D , the LNE dissolution must therefore stop at a finite LNE concentration. It is then instructive to inspect the variation of E_{Nernst} with composition, here for the example of Ag–Au. Since solid solutions of Ag and Au have practically no misfit strain energy, their molar enthalpy of mixing, Δh_{mix} , may be approximated by that of the molten alloy. Drop calorimetry data in ref 28 imply a nearly parabolic variation, $\Delta h_{\text{mix}} = -17.3\text{ kJ mol}^{-1}x(1-x)$, for the melt. When this term is adopted in a regular solution equation of state for solid Ag–Au, one obtains for the Ag chemical potential

$$\mu_{\text{Ag}} = \mu_{\text{Ag}}^0 + \Delta h_{\text{mix}} x_{\text{Au}}^2 + RT \ln(1 - x_{\text{Au}}) \quad (1)$$

and, consequently, for the Ag Nernst potential

$$E_{\text{Nernst}} = E_{\text{Nernst}}^0 - [\Delta h_{\text{mix}} x_{\text{Au}}^2 + RT \ln(1 - x_{\text{Au}})]/F \quad (2)$$

where the superscript “0” denotes values for pure Ag. R , T , and F denote, respectively, the gas constant, temperature, and Faraday constant. The equation yields an increase in E_{Nernst} by 63 mV between pure Ag and the equiatomic solution. Since the critical dealloying potentials are at $E_D \gtrsim E_{\text{Nernst}}^0 + 300\text{ mV}$, equilibrium thermodynamics cannot explain the observed LNE retention under the acting corrosion conditions. Yet, the increase of E_{Nernst} implies a reduction in overpotential which is significant if one accounts for the

kinetics of corrosion and specifically for the steep variation in the corrosion flux with the overpotential.

The above argument is consistent with the well-established variation of E_C with the alloy composition; see, for instance, ref 29 and the present results in Figure 2. The experimental observation here applies to corrosion which propagates throughout the material, in other words, to a macroscopic phenomenon. Nonetheless, it has been shown³⁰ that the empirical variation of E_C with the composition is consistent with results of an analysis at the microscopic scale, considering the atomic rearrangements in the corrosion surface. This analysis inspects the competition between dissolution on the one hand and passivation by lateral rearrangement of the more noble element on the other.³⁰ It then seems natural to assume that, as Ag dissolution enriches the outermost layer at the corrosion surface in Au, the potential required for maintaining dissolution at a significant rate will rise. Eventually, the corrosion process will become so slow as to effectively stop even before all less noble metal is dissolved.

Snyder and Erlebacher²⁰ have analyzed the kinetics of corrosion from a different atomistic perspective, taking the nucleation of vacancy islands on crystal terraces as the rate-limiting step. Their atomistic model implies that the overpotential required to maintain a given nucleation rate increases with the noble metal content, in agreement with the composition and overpotential dependence of the dissolution flux in their experiments in nonaqueous solution. The steady-state dissolution flux, J_{SS} , was found to vary with the composition as²⁰

$$J_{SS} \propto \exp \frac{E_T}{k_B T} \quad (3)$$

with the nucleation energy

$$E_T = 2.25 \text{ eV}x_{\text{Au}} + 0.53 \text{ eV}(1 - x_{\text{Au}}) \quad (4)$$

When applied to the temperature, 300 K, of our experiment, eqs 3 and 4 imply that J_{SS} decreases by the factor ~ 1000 whenever x_{Au} is increased by 10 atom %. This is again consistent with the kinetic stabilization of a significant LNE content when dealloying uses the low dealloying potentials that are feasible in dilute alloys. Note, however, that our reasoning is based on a *de facto* phenomenological application of a rate equation that, being based on vacancy island nucleation on a given alloy, contains in its derivation no mechanism to arrest the dissolution at final LNE content. Our argument is therefore not strictly self-consistent.

In summary, our discussion highlights the considerable LNE retention during the dealloying of dilute solid

solutions of the more noble element at low overpotential. We argue that this finding is qualitatively consistent with previous empirical data for the reduction of the corrosion rate and the increase of the critical dealloying potential when the initial LNE content is reduced. We point out that accounts of those latter findings based on atomistic models are also compatible with a trend for corrosion to slow down when the LNE content drops, preventing full LNE removal during finite time. Yet, while those same models connect to the removal of LNE on crystal terraces as the elemental corrosion step, they appear not to expose an atomic-scale process that would arrest the corrosion of any given terrace at a finite and substantial LNE content. In fact, the available theory does not afford a prediction of the amount of LNE retention at a given value of the dealloying potential and master alloy composition. Dedicated numerical studies of the phenomenon, along with detailed experiments on dilute alloy corrosion, would seem to be required for a clearer understanding of the factors that control LNE retention.

CONCLUSION

Our study demonstrates that dilute alloys of Au in Ag can be dealloyed at low overpotential so as to produce a massive nanoporous alloy in which roughly 50% of Ag is retained. We have shown that the microstructure of the alloy can be made to coarsen by annealing, and that the material can subsequently be subjected to a second dealloying step which removes the LNE almost completely, producing a “nested-network” nanoporous gold (N^3PG) structure that consists of self-similar, nested networks on two quite distinct length scales.

In view of the established phenomena of alloy corrosion, it appears natural to expect that, by control of the annealing and second dealloying conditions, both length scales can be independently tuned. Our two-step dealloying strategy can therefore enable the fabrication of hierarchical porous structure in bulk form with precise control over two levels of pore size.

N^3PG shows a faster charge transport rate than NPG, suggesting a faster switching in applications as a material with electrochemically tunable properties. In fact, we have shown that the nested-network microstructure of the material accelerates the signal transport into the pore space by more than 2 orders of magnitude, as compared to conventional nanoporous gold with comparable mass-specific surface area. Nested-network porous solids may therefore open the way to electrochemically functionalized materials that have a substantially improved response time and switching frequency.

METHODS

Master alloys $\text{Ag}_{(100-x)}\text{Au}_x$ with $x = 5, 10$, and 15 were arc melted from Ag (99.95%) and Au (99.995%) under argon

atmosphere and homogenized at 850°C for more than 100 h in evacuated and sealed quartz tubes. The ingots were then rolled, cut into cuboids $1 \times 1 \times 2 \text{ mm}^3$ in size using a wire saw, and annealed for recovery (650°C for 3 h).

The cuboid samples were dealloyed at room temperature ($\sim 20^\circ\text{C}$) under potential control in 1 M HClO_4 . The Pt wire counter electrode shared the cell (volume 300 mL) with the working electrode. Potentials were measured relative to Ag/AgCl reference electrodes in the same solution (530 mV positive of SHE). All potentials in this work are specified relative to Ag/AgCl. Coarsening treatments used a vacuum furnace at 10^{-6} mbar.

Reference samples of conventional NPG used a master alloy of $\text{Ag}_{75}\text{Au}_{25}$, dealloying potential of 750 mV for the single dealloying step, and otherwise identical procedures as above.

Anodic polarization curves were measured by positive-going potential sweeps from -300 to 600 mV at scan rate $\dot{E} = 1 \text{ mV s}^{-1}$. Chronoamperometry studies of electrochemical charging kinetics started with a 600 s hold at the initial potential, E_0 , before the jump to the final potential, E_f .

Structural characterization used a scanning electron microscope (SEM, LEO 1530), and composition analysis was performed in the SEM using energy-dispersive X-ray spectroscopy (EDS, Oxford INCA). The specific surface area was characterized by the capacitance ratio method,²⁴ using 1 M HClO_4 as the electrolyte and an NPG sample as the counter electrode. The capacitance value, c , of Au in the double-layer region of the voltammogram was taken as $c_{\text{dl}} = 40 \mu\text{F cm}^{-2}$.³¹ With m the sample mass, the current, I , was taken to obey $I = c_{\text{dl}}\alpha_m m\dot{E}$ which, all other quantities being known, can be solved for the mass-specific surface area, α_m .

Conflict of Interest: The authors declare no competing financial interest.

Acknowledgment. Support by Chinese Scholarship Council (Z.Q.) and by Deutsche Forschungsgemeinschaft (SFB 986 "M³" project B2) is gratefully acknowledged. We thank Dr. H. Jin (Shenyang National Laboratory for Materials Science) for useful discussion, Y. Xue (HZG) for advice on the charging experiments, and Dr. M. Ritter (SFB 986 project Z3) for assistance with scanning electron microscopy.

REFERENCES AND NOTES

- Li, R.; Sieradzki, K. Ductile-Brittle Transition in Random Porous Au. *Phys. Rev. Lett.* **1992**, *68*, 1168–1171.
- Erlebacher, J.; Aziz, M. J.; Karma, A.; Dimitrov, N.; Sieradzki, K. Evolution of Nanoporosity in Dealloying. *Nature* **2001**, *410*, 450–453.
- Weissmüller, J.; Newman, R. C.; Jin, H. J.; Hodge, A. M.; Kysar, J. W. Nanoporous Metals by Alloy Corrosion: Formation and Mechanical Properties. *MRS Bull.* **2009**, *34*, 577–586.
- Kramer, D.; Viswanath, R. N.; Weissmüller, J. Surface-Stress Induced Macroscopic Bending of Nanoporous Gold Cantilevers. *Nano Lett.* **2004**, *4*, 793–796.
- Biener, J.; Wittstock, A.; Zepeda-Ruiz, L. A.; Biener, M. M.; Zielasek, V.; Kramer, D.; Viswanath, R. N.; Weissmüller, J.; Bäumer, M.; Hamza, A. V. Surface-Chemistry-Driven Actuation in Nanoporous Gold. *Nat. Mater.* **2009**, *8*, 47–51.
- Jin, H. J.; Wang, X. L.; Parida, S.; Wang, K.; Seo, M.; Weissmüller, J. Nanoporous Au–Pt Alloys as Large Strain Electrochemical Actuators. *Nano Lett.* **2010**, *10*, 187–194.
- Jin, H. J.; Weissmüller, J. A Material with Electrically Tunable Strength and Flow Stress. *Science* **2011**, *332*, 1179–1182.
- Wahl, P.; Traussnig, T.; Landgraf, S.; Jin, H. J.; Weissmüller, J.; Würschum, R. Adsorption-Driven Tuning of the Electrical Resistance of Nanoporous Gold. *J. Appl. Phys.* **2010**, *108*, 073706.
- Ding, Y.; Chen, M. W. Nanoporous Metals for Catalytic and Optical Applications. *MRS Bull.* **2009**, *34*, 569–576.
- Snyder, J.; Fujita, T.; Chen, M. W.; Erlebacher, J. Oxygen Reduction in Nanoporous Metal-Ionic Liquid Composite Electrocatalysts. *Nat. Mater.* **2010**, *9*, 904–907.
- Wittstock, A.; Zielasek, V.; Biener, J.; Friend, C. M.; Bäumer, M. Nanoporous Gold Catalysts for Selective Gas-Phase Oxidative Coupling of Methanol at Low Temperature. *Science* **2010**, *327*, 319–322.
- Wang, L. C.; Zhong, Y.; Jin, H. J.; Widmann, D.; Weissmüller, J.; Behm, R. J. On the Role of Residual Ag in Nanoporous Au Catalysts for CO Oxidation: A Combined Microreactor and TAP Reactor Study. *ChemCatChem* **2012**, *4*, 251–259.
- Zhang, Z. H.; Wang, Y.; Qi, Z.; Lin, J. K.; Bian, X. F. Nanoporous Gold Ribbons with Bimodal Channel Size Distributions by Chemical Dealloying of Al–Au Alloys. *J. Phys. Chem. C* **2009**, *113*, 1308–1314.
- Wang, X. G.; Sun, J. Z.; Zhang, C.; Kou, T. Y.; Zhang, Z. H. On the Microstructure, Chemical Composition, and Porosity Evolution of Nanoporous Alloy through Successive Dealloying of Ternary Al–Pd–Au Precursor. *J. Phys. Chem. C* **2012**, *116*, 13271–13280.
- Ding, Y.; Erlebacher, J. Nanoporous Metals with Controlled Multimodal Pore Size Distribution. *J. Am. Chem. Soc.* **2003**, *125*, 7772–7773.
- Xing, X. F.; Han, D. Q.; Wu, Y. F.; Guan, Y.; Bao, N.; Xu, X. H. Fabrication and Electrochemical Property of Hierarchically Porous Au–Cu Films. *Mater. Lett.* **2012**, *71*, 108–110.
- Biener, J.; Nyce, G. W.; Hodge, A. M.; Biener, M. M.; Hamza, A. V.; Maier, S. A. Nanoporous Plasmonic Metamaterials. *Adv. Mater.* **2008**, *20*, 1211–1217.
- Pickering, H. W. Characteristic Features of Alloy Polarization Curves. *Corros. Sci.* **1983**, *23*, 1107–1120.
- Sieradzki, K.; Dimitrov, N.; Movrin, D.; McCall, C.; Vasiljevic, N.; Erlebacher, J. The Dealloying Critical Potential. *J. Electrochem. Soc.* **2002**, *149*, B370–B377.
- Snyder, J.; Erlebacher, J. Kinetics of Crystal Etching Limited by Terrace Dissolution. *J. Electrochem. Soc.* **2010**, *157*, C125–C130.
- Erlebacher, J. An Atomistic Description of Dealloying. *J. Electrochem. Soc.* **2004**, *151*, C614–C626.
- Dursun, A.; Pugh, D. V.; Corcoran, S. G. Dealloying of Ag–Au Alloys in Halide-Containing Electrolytes Affect on Critical Potential and Pore Size. *J. Electrochem. Soc.* **2003**, *150*, B355–B360.
- Parida, S.; Kramer, D.; Volkert, C. A.; Rösner, H.; Erlebacher, J.; Weissmüller, J. Volume Change during the Formation of Nanoporous Gold by Dealloying. *Phys. Rev. Lett.* **2006**, *97*, 035504.
- Trasatti, S.; Petrii, A. Real Surface Area Measurements in Electrochemistry. *Pure Appl. Chem.* **1991**, *63*, 711–734.
- Richer, J.; Lipkowski, J. Measurement of Physical Adsorption of Neutral Organic Species at Solid Electrodes. *J. Electrochem. Soc.* **1986**, *131*, 121–128.
- Ateya, B. G.; Fritz, J. D.; Pickering, H. W. Kinetics of Dealloying of a Copper-5 Atomic Percent Gold Alloy. *J. Electrochem. Soc.* **1997**, *144*, 2606–2613.
- Ateya, B. G.; Geh, G.; Carim, A. H.; Pickering, H. W. Selective Dissolution below the Critical Potential and Back Alloying in Copper–Gold Alloy. *J. Electrochem. Soc.* **2002**, *149*, B27–B33.
- Fitzner, K.; Guo, Q. T.; Wang, J. W.; Kleppa, O. J. Enthalpies of Liquid–Liquid Mixing in the Systems Cu–Ag, Cu–Au and Ag–Au by Using an *In-Situ* Mixing Device in a High Temperature Single-Unit Differential Calorimeter. *J. Alloys Compd.* **1999**, *291*, 190–200.
- Newman, R. C.; Corcoran, S. G.; Erlebacher, J.; Aziz, M. J.; Sieradzki, K. Alloy Corrosion. *MRS Bull.* **1999**, *24*, 24–28.
- Erlebacher, J.; Sieradzki, K. Pattern Formation during Dealloying. *Scripta Mater.* **2003**, *49*, 991–996.
- Germain, P. S.; Pell, W. G.; Conway, B. E. Evaluation and Origins of the Difference between Double-Layer Capacitance Behaviour at Au-Metal and Oxidized Au Surface. *Electrochim. Acta* **2004**, *49*, 1775–1788.